

A spectral-element discontinuous Galerkin thermal lattice Boltzmann method for conjugate heat transfer applications

Saamil Patel¹, Misun Min² and Taehun Lee^{1,*},[†]

¹*Department of Mechanical Engineering, City College of City University of New York, New York, NY 10031, USA*

²*Mathematics and Computer Science Division, Argonne National Laboratory, Argonne, IL 60439, USA*

SUMMARY

We present a spectral-element discontinuous Galerkin thermal lattice Boltzmann method for fluid–solid conjugate heat transfer applications. Using the discrete Boltzmann equation, we propose a numerical scheme for conjugate heat transfer applications on unstructured, non-uniform grids. We employ a double-distribution thermal lattice Boltzmann model to resolve flows with variable Prandtl (Pr) number. Based upon its finite element heritage, the spectral-element discontinuous Galerkin discretization provides an effective means to model and investigate thermal transport in applications with complex geometries. Our solutions are represented by the tensor product basis of the one-dimensional Legendre–Lagrange interpolation polynomials. A high-order discretization is employed on body-conforming hexahedral elements with Gauss–Lobatto–Legendre quadrature nodes. Thermal and hydrodynamic bounce-back boundary conditions are imposed via the numerical flux formulation that arises because of the discontinuous Galerkin approach. As a result, our scheme does not require tedious extrapolation at the boundaries, which may cause loss of mass conservation. We compare solutions of the proposed scheme with an analytical solution for a solid–solid conjugate heat transfer problem in a 2D annulus and illustrate the capture of temperature continuities across interfaces for conductivity ratio $\gamma > 1$. We also investigate the effect of Reynolds (Re) and Grashof (Gr) number on the conjugate heat transfer between a heat-generating solid and a surrounding fluid. Steady-state results are presented for $Re = 5 - 40$ and $Gr = 10^5 - 10^6$. In each case, we discuss the effect of Re and Gr on the heat flux (i.e. Nusselt number Nu) at the fluid–solid interface. Our results are validated against previous studies that employ finite-difference and continuous spectral-element methods to solve the Navier–Stokes equations. Copyright © 2016 John Wiley & Sons, Ltd.

Received 28 December 2015; Revised 20 April 2016; Accepted 23 April 2016

KEY WORDS: conjugate heat transfer; spectral-element method; discontinuous Galerkin method; Lattice Boltzmann method

1. INTRODUCTION

Conjugate heat transfer (CHT) occurs when heat is transferred between two different mediums that are in contact with each other. The process is observed in numerous engineering applications: the drying of different materials (paper, steel, and glass), food processing, cooling of electronic circuits, and nuclear reactor processes. These examples generally involve a fluid that is convected over a solid surface. Predicting the flow and temperature fields for CHT by means of computational fluid dynamics solvers can be a difficult task, especially in complex geometries like a nuclear reactor core [1]. Another difficulty is to maintain the continuity of temperature and heat fluxes at the fluid–solid interface. While traditional computational fluid dynamics methods [2, 3] have proven successful in enforcing such boundary conditions, there is considerable computational cost associated with the implementation [4].

*Correspondence to: Taehun Lee, Department of Mechanical Engineering, City College of City University of New York, New York, NY 10031, USA.

[†]E-mail: thlee@ccny.cuny.edu

Incompressible flow past an isothermal circular cylinder and the associated convection heat transfer have been the subject of numerous research articles. This problem is of particular importance because it exhibits a rich and complicated flow structure around a relatively simple geometry. Yet, from a computational perspective, the geometry requires a careful arrangement of the mesh in order to capture the onset of the von Kármán vortex street. Jain and Goel [5] were one of the first to numerically investigate this problem using a finite-difference method. Later, using a spectral element method, Karniadakis [2] simulated forced convection heat transfer from an isolated cylinder in a cross-flow for Reynolds number $Re = 200$. A thorough review of the early numerical and experimental studies can be found in [3].

Many of these studies treat the cylinder with a prescribed constant temperature Dirichlet boundary condition, revealing no analysis on the heat exchange between the flow and interior of the cylinder. Understanding how the flow affects the temperature distribution *within* the cylinder has been the subject of some recent studies. Juncu [6] reported cylinder temperatures for $Re = 2$ and $Re = 20$. Das and Reddy [7] investigated natural convection flow in a square enclosure with a central solid conducting body where they use a finite-volume scheme to discretize the energy equations within the flow and solid regions. Others, like Jeon *et al.* [8] and Sambamurthy *et al.* [9], have investigated both natural and forced convection heat transfer, using finite-element and finite-difference methods, where the solid conducting body now had a volumetric heat source.

The lattice Boltzmann method (LBM) [10] has emerged as a reliable method for simulating thermal flows, and a thorough review of the relevant work can be found in [11, 12]. There are a few studies that have investigated fluid–solid CHT via the LBM. Wang *et al.* [4] proposed a double-distribution model that insured temperature and heat flux continuity at the fluid–solid interface. Yet, the scope of their applications was limited to simple Cartesian box geometries. Jami *et al.* [13] investigated natural convection with a heat-generating cylinder conducting body using a multiple-relaxation-time LBM to capture the flow field while using a macroscopic energy equation to resolve the temperature field. Yan and Zu [14] investigated flow past a rotating isothermal circular cylinder. Their work also incorporated a double-distribution model with a regular lattice grid that requires a complex treatment to impose the hydrodynamic boundary conditions on a curved cylinder surface. In addition, thermal boundary conditions were realized through an extrapolation method that can sometimes lead to errors in conservation laws [15]. While these studies have been able to provide accurate and reasonable results, severe limitations persist when using regular Cartesian grids to capture the flow physics around curved or irregular boundaries. Considerable efforts for solving the discrete Boltzmann equation (DBE) on irregular grids have been published, and we refer the reader to [15] to learn more.

The aim of this work is to propose a thermal LBM (TLBM) for CHT problems that can capture heat transfer across a geometrically complex boundary between a fluid and solid that are in perfect contact. We adopt a double-distribution model [16, 17], where the DBE for the density distribution function is solved to determine the momentum field and a thermal DBE (TDBE) for the internal energy distribution function is solved to determine the passive temperature field. Both equations are solved via a splitting scheme that is composed of a collision and streaming (linear advection) step. Our numerical scheme is based on the work of Min and Lee [15] who discretized the streaming step of the solution procedure using a spectral-element discontinuous Galerkin (SEDG) method. The approach benefits from a high-order spectral discretization that is based on the tensor product basis given by the one-dimensional Legendre–Lagrange interpolation polynomials. As a result of choosing the SEDG discretization, we benefit from incorporating body-conforming hexahedral elements to mesh the computational domain and lay the groundwork to tackle future problems with more complex geometries. An additional advantage is the simple application of the bounce-back boundary condition through the numerical flux (an artifact of the discontinuous Galerkin approach). We can apply the bounce-back condition in an effortless manner that does not call for further extrapolation or interpolation techniques as is carried out when using a regular Cartesian lattice for complex geometries. The continuity of temperature and heat flux across the fluid–solid interface is easily enforced by treating the temperature field in the entire computational domain as a continuous field. Abrupt changes in thermal conductivity across the fluid–solid interface are properly reflected in the relaxation terms of the collision step. Numerical results on forced and natural convection of flow

surrounding a heat-generating solid are presented with this model. As a first step, we present steady-state results for $Re = 5 - 40$ and $Gr = 10^5 - 10^6$. In the case of forced convection, results are compared with those provided by Nek5000 [18], an open-source Navier–Stokes solver based on the spectral element method. Natural convection results are compared with the work of Sambamurthy *et al.* [9], who employed a finite difference method.

The paper is organized as follows. In Section 2, we present the governing equations, namely, the thermal lattice Boltzmann equations (TLBE) for nearly incompressible fluids that resolves the density, momentum, and temperature fields. In Section 3, we discuss the numerical discretization of our scheme. Section 4 presents computational results that include a comparison of the proposed scheme and an analytical solution for CHT between two solids in perfect contact. Following this, we present simulations of forced and natural convection flows around heat-generating bodies. We discuss our conclusions in Section 5. Details on the thermal boundary conditions are given in the Appendix.

2. GOVERNING EQUATIONS

In this section, we describe the governing equations for CHT between nearly incompressible fluids and solids. Our formulation is a passive scalar approach and uses an additional evolution equation for internal energy to describe temperature.

2.1. Thermal discrete Boltzmann equations for nearly incompressible flows

The TDBEs with the Bhatnagar–Gross–Krook collision model [19] are written in the following way:

$$\frac{\partial f_\alpha}{\partial t} + \mathbf{e}_\alpha \cdot \nabla f_\alpha = -\frac{f_\alpha - f_\alpha^{eq}}{\lambda_f} + \frac{(\mathbf{e}_\alpha - \mathbf{u}) \cdot \mathbf{F} f_\alpha^{eq}}{\rho c_s^2} \quad (1)$$

$$\frac{\partial g_\alpha}{\partial t} + \mathbf{e}_\alpha \cdot \nabla g_\alpha = -\frac{g_\alpha - g_\alpha^{eq}}{\lambda_g} + t_\alpha \dot{Q} \quad (2)$$

where

$$g_\alpha = \frac{(\mathbf{e}_\alpha - \mathbf{u})^2}{2} f_\alpha \quad (3)$$

These equations reflect the approach of He *et al.* [17] and introduce the internal energy distribution function (g_α) to resolve the internal energy. The density and momentum fields are simulated using the density distribution function (f_α). As it is noted in [17] and [20], the second moment of f yields a fixed Prandtl number, which means that the thermal conductivity cannot be adjusted independent of the kinetic viscosity. Using the representation given by Eq. (3), He *et al.* [17] sought to investigate thermal flows with variable Prandtl number. Given their work, we do not use the density distribution function to calculate the internal energy. In addition, Eq. (2) follows from the simplifications of Peng *et al.* [21], where viscous heat dissipation and compression work by pressure are neglected. f_α and g_α ($\alpha = 0, 1, \dots, N_\alpha$) are the particle density and internal energy distribution functions, respectively. Each is defined in the direction of the microscopic velocity \mathbf{e}_α where N_α is the number of microscopic velocities. λ_f and λ_g are the relaxation times related to momentum diffusion and energy transport, respectively. The second term on the right-hand side of Eq. (1) represents the force term where \mathbf{F} is an external body force that depends on space and time. \dot{Q} is a constant volumetric heat generation term. We consider the two-dimensional nine-velocity model (D2Q9) associated with $\mathbf{e}_\alpha = (0, 0)$ for $\alpha = 0$; $\mathbf{e}_\alpha = (\cos \theta_\alpha, \sin \theta_\alpha)$ with $\theta_\alpha = (\alpha - 1)\pi/2$ for $\alpha = 1, 2, 3, 4$; and $\mathbf{e}_\alpha = \sqrt{2}(\cos \phi_\alpha, \sin \phi_\alpha)$ with $\phi_\alpha = (\alpha - 5)\pi/2 + \pi/4$ for $\alpha = 5, 6, 7, 8$.

The equilibrium distribution functions are given by

$$f_\alpha^{eq} = t_\alpha \rho \left[1 + \frac{(\mathbf{e}_\alpha \cdot \mathbf{u})}{c_s^2} + \frac{(\mathbf{e}_\alpha \cdot \mathbf{u})^2}{2c_s^4} - \frac{(\mathbf{u} \cdot \mathbf{u})}{2c_s^2} \right], \quad (4)$$

and

$$g_\alpha^{eq} = t_\alpha \rho e \left[\omega_\alpha^1 + \omega_\alpha^2 \frac{(\mathbf{e}_\alpha \cdot \mathbf{u})}{c_s^2} + \frac{(\mathbf{e}_\alpha \cdot \mathbf{u})^2}{2c_s^4} - \frac{(\mathbf{u} \cdot \mathbf{u})}{2c_s^2} \right], \quad (5)$$

where ρ is the density of the fluid; e is the internal energy; \mathbf{u} is the macroscopic velocity; $t_0 = 4/9$, $t_{\alpha=1,4} = 1/9$, and $t_{\alpha=5,8} = 1/36$ are the weights; $\omega_0^1 = \omega_0^2 = 0$, $\omega_{\alpha=1,4}^1 = \omega_{\alpha=1,4}^2 = 3/2$, $\omega_{\alpha=5,8}^1 = 3$, and $\omega_{\alpha=5,8}^2 = 6$; and $c_s = 1/\sqrt{3}$ is the speed of sound [22].

2.2. Thermal lattice Boltzmann equations for nearly incompressible fluids

The TLBE is obtained by discretizing Eqs (1) and (2) along characteristics over a time-step δt as shown in [12, 15]

$$f_\alpha(\mathbf{x}, t) - f_\alpha(\mathbf{x} - \mathbf{e}_\alpha \delta t, t - \delta t) = - \int_{t-\delta t}^t \frac{f_\alpha - f_\alpha^{eq}}{\lambda_f} dt' + \int_{t-\delta t}^t \frac{(\mathbf{e}_\alpha - \mathbf{u}) \cdot \mathbf{F} f_\alpha^{eq}}{\rho c_s^2} dt', \quad (6)$$

$$g_\alpha(\mathbf{x}, t) - g_\alpha(\mathbf{x} - \mathbf{e}_\alpha \delta t, t - \delta t) = - \int_{t-\delta t}^t \frac{g_\alpha - g_\alpha^{eq}}{\lambda_g} dt' + \int_{t-\delta t}^t t_\alpha \dot{Q} dt'. \quad (7)$$

We note that this temporal integration $[t - \delta t, t]$ is coupled with the space integration $[\mathbf{x} - \mathbf{e}_\alpha \delta t, \mathbf{x}]$. Applying the trapezoidal rule [23] for the integration on the right-hand side of Eqs (6) and (7), we have the following for each term

$$\begin{aligned} \int_{t-\delta t}^t \frac{f_\alpha - f_\alpha^{eq}}{\lambda_f} dt' &\approx \frac{f_\alpha - f_\alpha^{eq}}{2\tau_f} \Big|_{(\mathbf{x}-\mathbf{e}_\alpha \delta t, t-\delta t)} + \frac{f_\alpha - f_\alpha^{eq}}{2\tau_f} \Big|_{(\mathbf{x}, t)} \\ \int_{t-\delta t}^t \frac{(\mathbf{e}_\alpha - \mathbf{u}) \cdot \mathbf{F} f_\alpha^{eq}}{\rho c_s^2} dt' &\approx \delta t \frac{(\mathbf{e}_\alpha - \mathbf{u}) \cdot \mathbf{F} f_\alpha^{eq}}{2\rho c_s^2} \Big|_{(\mathbf{x}-\mathbf{e}_\alpha \delta t, t-\delta t)} + \delta t \frac{(\mathbf{e}_\alpha - \mathbf{u}) \cdot \mathbf{F} f_\alpha^{eq}}{2\rho c_s^2} \Big|_{(\mathbf{x}, t)}, \quad (8) \\ \int_{t-\delta t}^t \frac{g_\alpha - g_\alpha^{eq}}{\lambda_g} dt' &\approx \frac{g_\alpha - g_\alpha^{eq}}{2\tau_g} \Big|_{(\mathbf{x}-\mathbf{e}_\alpha \delta t, t-\delta t)} + \frac{g_\alpha - g_\alpha^{eq}}{2\tau_g} \Big|_{(\mathbf{x}, t)} \end{aligned}$$

$$\int_{t-\delta t}^t t_\alpha \dot{Q} dt' \approx \frac{\delta t}{2} t_\alpha \dot{Q} \Big|_{(\mathbf{x}-\mathbf{e}_\alpha \delta t, t-\delta t)} + \frac{\delta t}{2} t_\alpha \dot{Q} \Big|_{(\mathbf{x}, t)}. \quad (9)$$

where the dimensionless relaxation times are $\tau_f = \lambda_f/\delta t$ and $\tau_g = \lambda_g/\delta t$. A relation to the kinematic viscosity and thermal diffusivity is given by $\nu = \tau_f c_s^2 \delta t$ and $\chi = \frac{(D+2)\tau_g c_s^2 \delta t}{D}$ (D is the dimension of the problem).

Using Eqs (2.2) and (9), we can now write Eqs (6) and (7) as the TLBE for a single-phase nearly incompressible fluid:

$$\begin{aligned} \bar{f}_\alpha(\mathbf{x}, t) &= \bar{f}_\alpha(\mathbf{x} - \mathbf{e}_\alpha \delta t, t - \delta t) - \frac{1}{\tau_f + 1/2} (\bar{f}_\alpha - \bar{f}_\alpha^{eq}) \Big|_{(\mathbf{x}-\mathbf{e}_\alpha \delta t, t-\delta t)} \\ &\quad + \delta t \frac{(\mathbf{e}_\alpha - \mathbf{u}) \cdot \mathbf{F} f_\alpha^{eq}}{\rho c_s^2} \Big|_{(\mathbf{x}-\mathbf{e}_\alpha \delta t, t-\delta t)}. \quad (10) \end{aligned}$$

$$\bar{g}_\alpha(\mathbf{x}, t) = \bar{g}_\alpha(\mathbf{x} - \mathbf{e}_\alpha \delta t, t - \delta t) - \frac{1}{\tau_g + 1/2} (\bar{g}_\alpha - \bar{g}_\alpha^{eq}) \Big|_{(\mathbf{x}-\mathbf{e}_\alpha \delta t, t-\delta t)} + \delta t \dot{Q} t_\alpha, \quad (11)$$

where \bar{f}_α , \bar{g}_α , \bar{f}_α^{eq} and \bar{g}_α^{eq} are the modified particle and equilibrium distribution functions for the density and internal energy distribution functions. They are defined as

$$\bar{f}_\alpha = f_\alpha + \frac{f_\alpha - f_\alpha^{eq}}{2\tau_f} - \frac{(\mathbf{e}_\alpha - \mathbf{u}) \cdot \mathbf{F} f_\alpha^{eq}}{2\rho c_s^2} \quad (12)$$

$$\bar{f}_\alpha^{eq} = f_\alpha^{eq} - \frac{(\mathbf{e}_\alpha - \mathbf{u}) \cdot \mathbf{F} f_\alpha^{eq}}{2\rho c_s^2} \tag{13}$$

$$\bar{g}_\alpha = g_\alpha + \frac{g_\alpha - g_\alpha^{eq}}{2\tau_g} - \frac{\delta t}{2} t_\alpha \dot{Q} \tag{14}$$

$$\bar{g}_\alpha^{eq} = g_\alpha^{eq} - \frac{\delta t}{2} t_\alpha \dot{Q} \tag{15}$$

Equations (10) and (11) are then solved in two steps:

• **Collision**

$$\begin{aligned} \bar{f}_\alpha^*(\mathbf{x}, t - \delta t) &= \bar{f}_\alpha(\mathbf{x}, t - \delta t) - \frac{1}{\tau_f + 1/2} (\bar{f}_\alpha - \bar{f}_\alpha^{eq}) \Big|_{(\mathbf{x}, t - \delta t)} \\ &\quad + \delta t \frac{(\mathbf{e}_\alpha - \mathbf{u}) \cdot \mathbf{F} f_\alpha^{eq}}{\rho c_s^2} \Big|_{(\mathbf{x}, t - \delta t)} \end{aligned} \tag{16}$$

$$\begin{aligned} \bar{g}_\alpha^*(\mathbf{x}, t - \delta t) &= \bar{g}_\alpha(\mathbf{x}, t - \delta t) - \frac{1}{\tau_g + 1/2} (\bar{g}_\alpha - \bar{g}_\alpha^{eq}) \Big|_{(\mathbf{x}, t - \delta t)} \\ &\quad + t_\alpha \dot{Q} \delta t \Big|_{(\mathbf{x}, t - \delta t)}, \end{aligned} \tag{17}$$

which is followed by the substitutions $\bar{f}_\alpha(\mathbf{x}, t - \delta t) = \bar{f}_\alpha^*(\mathbf{x}, t - \delta t)$ and $\bar{g}_\alpha(\mathbf{x}, t - \delta t) = \bar{g}_\alpha^*(\mathbf{x}, t - \delta t)$.

• **Streaming**

$$\bar{f}_\alpha(\mathbf{x}, t) = \bar{f}_\alpha(\mathbf{x} - \mathbf{e}_\alpha \delta t, t - \delta t). \tag{18}$$

$$\bar{g}_\alpha(\mathbf{x}, t) = \bar{g}_\alpha(\mathbf{x} - \mathbf{e}_\alpha \delta t, t - \delta t). \tag{19}$$

The streaming step of Eqs (18) and (19) can be expressed as a solution of the linear advection equation, written in an Eulerian framework [24]:

$$\frac{\partial \bar{f}_\alpha}{\partial t} + \mathbf{e}_\alpha \cdot \nabla \bar{f}_\alpha = 0. \tag{20}$$

$$\frac{\partial \bar{g}_\alpha}{\partial t} + \mathbf{e}_\alpha \cdot \nabla \bar{g}_\alpha = 0. \tag{21}$$

The density, momentum, and temperature can be computed by taking moments as follows:

$$\rho = \sum_{\alpha=0}^{N_\alpha} \bar{f}_\alpha \quad \text{and} \quad \rho \mathbf{u} = \sum_{\alpha=0}^{N_\alpha} \mathbf{e}_\alpha \bar{f}_\alpha + \frac{\delta t}{2} \mathbf{F} \quad \text{and} \quad \rho e = \sum_{\alpha=0}^{N_\alpha} \bar{g}_\alpha + \frac{\delta t}{2} \dot{Q} \tag{22}$$

where e , the internal energy, is related to the temperature by $e = DRT/2$ where D is the dimension and R is the gas constant.

3. NUMERICAL DISCRETIZATION

In this section, we present our computational scheme. We provide details to the discontinuous Galerkin strong formulation, numerical fluxes, and boundary conditions for Eqs (20) and (21). Details on the spectral element discretization are also discussed.

3.1. Weak formulation of LB advection equation

We formulate the weak form for Eqs (20) and (21) defined on the computational domain $\Omega = \cup_{e=1}^E \Omega^e$ with non-overlapping elements Ω^e . We begin by writing the global solutions, $\bar{f}_\alpha(\mathbf{x}, t)$ and $\bar{g}_\alpha(\mathbf{x}, t)$, which will be approximated by the piecewise N -th order polynomial approximations, $\bar{f}_\alpha(\mathbf{x}, t)_h$ and $\bar{g}_\alpha(\mathbf{x}, t)_h$,

$$\begin{aligned} \bar{f}_\alpha(\mathbf{x}, t) &\simeq \bar{f}_\alpha(\mathbf{x}, t)_h = \oplus_{e=1}^E \bar{f}_\alpha(\mathbf{x}, t)_h^e \\ \bar{g}_\alpha(\mathbf{x}, t) &\simeq \bar{g}_\alpha(\mathbf{x}, t)_h = \oplus_{e=1}^E \bar{g}_\alpha(\mathbf{x}, t)_h^e \end{aligned} \tag{23}$$

where the subscript h refers to a characteristic measure of the size of the element, Ω^e . $\bar{f}_\alpha(\mathbf{x}, t)_h^e$ and $\bar{g}_\alpha(\mathbf{x}, t)_h^e$ represent the local polynomial solution on the element Ω^e . The next step is to define a global space $V_{\alpha,h}$ of test functions, $\phi_{\alpha,h}$, such that $V_{\alpha,h} = \oplus_{e=1}^E V_{\alpha,h}^e$. The locally defined spaces $V_{\alpha,h}^e$ are defined by $V_{\alpha,h}^e = span \left\{ \phi_{\alpha,h}^n \right\}_{n=1}^{N_p}$. Another way to describe $V_{\alpha,h}^e$ is the set of all linear combinations of $\phi_{\alpha,h}^n$, where N_p is the number of quadrature points that are defined on the element Ω^e . Details on the functional form of the test functions, $\phi_{\alpha,h}^n$, are given later in this paper. For now, we indicate that our locally defined solutions $\bar{f}_\alpha(\mathbf{x}, t)_h^e$ and $\bar{g}_\alpha(\mathbf{x}, t)_h^e$ are polynomials that are written as an expansion of the test functions:

$$\begin{aligned} \bar{f}_\alpha(\mathbf{x}, t)_h^e &= \sum_i^{N_p} (\bar{f}_\alpha^i(t)) \phi_{\alpha,h}^i(\mathbf{x}) \\ \bar{g}_\alpha(\mathbf{x}, t)_h^e &= \sum_i^{N_p} (\bar{g}_\alpha^i(t)) \phi_{\alpha,h}^i(\mathbf{x}) \end{aligned} \tag{24}$$

With properly defined test functions $\phi_{\alpha,h}$, we multiply them with Eqs (20) and (21) and integrate by parts twice in a manner similar to [15], where we then obtain the following weak formulations:

$$\left(\frac{\partial \bar{f}_\alpha}{\partial t} + \nabla \cdot \mathbf{F}_\alpha(\bar{f}), \phi_{\alpha,h} \right)_{\Omega^e} = (\mathbf{n} \cdot [\mathbf{F}_\alpha(\bar{f}) - \mathbf{F}_\alpha^*(\bar{f})], \phi_{\alpha,h})_{\partial\Omega^e} \tag{25}$$

$$\left(\frac{\partial \bar{g}_\alpha}{\partial t} + \nabla \cdot \mathbf{G}_\alpha(\bar{g}), \phi_{\alpha,h} \right)_{\Omega^e} = (\mathbf{n} \cdot [\mathbf{G}_\alpha(\bar{g}) - \mathbf{G}_\alpha^*(\bar{g})], \phi_{\alpha,h})_{\partial\Omega^e} \tag{26}$$

where $\mathbf{F}_\alpha(\bar{f}) = \mathbf{e}_\alpha \bar{f}_\alpha$ and $\mathbf{G}_\alpha(\bar{g}) = \mathbf{e}_\alpha \bar{g}_\alpha$ represent the flux vectors for the density distribution function and internal energy distribution function, respectively. $\mathbf{e}_\alpha = (e_{\alpha x}, e_{\alpha y})$ are the microscopic velocities, and $\mathbf{n} = (n_x, n_y)$ is the unit normal vector pointing outward on the element boundary, $\partial\Omega^e$. The numerical fluxes $\mathbf{F}_\alpha^*(\bar{f}) = \mathbf{F}_\alpha^*(\bar{f}, \bar{f}^+)$ and $\mathbf{G}_\alpha^*(\bar{g}) = \mathbf{G}_\alpha^*(\bar{g}, \bar{g}^+)$ in Eqs (25) and (26) are a function of the local solution (i.e., $\bar{f}_\alpha, \bar{g}_\alpha$) and the neighboring solution (i.e., $\bar{f}_\alpha^+, \bar{g}_\alpha^+$) at the interfaces between neighboring elements. We choose the Lax–Friedrichs flux in [15, 25], which gives the following form for the integrand in the surface integrals of Eqs (25) and (26):

$$\begin{aligned} \mathbf{n} \cdot (\mathbf{F}_\alpha - \mathbf{F}_\alpha^*) &= \begin{cases} (\mathbf{n} \cdot \mathbf{e}_\alpha) [\bar{f}_\alpha - \bar{f}_\alpha^+] & \text{for } \mathbf{n} \cdot \mathbf{e}_\alpha < 0, \\ 0 & \text{for } \mathbf{n} \cdot \mathbf{e}_\alpha \geq 0. \end{cases} \\ \mathbf{n} \cdot (\mathbf{G}_\alpha - \mathbf{G}_\alpha^*) &= \begin{cases} (\mathbf{n} \cdot \mathbf{e}_\alpha) [\bar{g}_\alpha - \bar{g}_\alpha^+] & \text{for } \mathbf{n} \cdot \mathbf{e}_\alpha < 0, \\ 0 & \text{for } \mathbf{n} \cdot \mathbf{e}_\alpha \geq 0. \end{cases} \end{aligned} \tag{27}$$

When $\mathbf{n} \cdot \mathbf{e}_\alpha < 0$, we can write

$$\begin{aligned} \mathbf{n} \cdot (\mathbf{F}_\alpha - \mathbf{F}_\alpha^*) &= (n_x e_{\alpha x} + n_y e_{\alpha y}) \bar{f}_\alpha + (n_x^+ e_{\alpha x} + n_y^+ e_{\alpha y}) \bar{f}_\alpha^+ \\ \mathbf{n} \cdot (\mathbf{G}_\alpha - \mathbf{G}_\alpha^*) &= (n_x e_{\alpha x} + n_y e_{\alpha y}) \bar{g}_\alpha + (n_x^+ e_{\alpha x} + n_y^+ e_{\alpha y}) \bar{g}_\alpha^+ \end{aligned} \tag{28}$$

The proper upwinding scheme, inherent in the Lax–Friedrichs flux, allows momentum transfer at the element interface to depend only on those particles that are entering into the element.

3.2. Boundary conditions

Boundary conditions are weakly imposed through the numerical flux. The hydrodynamic wall boundary condition, with specific details provided in [15, 26], is given as follows:

$$\bar{f}_\alpha - \bar{f}_\alpha^+ = \begin{cases} \bar{f}_\alpha - \bar{f}_{\alpha^*} - 2t_\alpha \rho_0 (\mathbf{e}_\alpha \cdot \mathbf{u}_b) / c_s^2 & \text{for } \mathbf{n} \cdot \mathbf{e}_\alpha < 0 \\ 0 & \text{for } \mathbf{n} \cdot \mathbf{e}_\alpha \geq 0, \end{cases} \quad (29)$$

where \bar{f}_{α^*} is the particle distribution function moving in the opposite direction of \bar{f}_α , \mathbf{u}_b is the macroscopic velocity prescribed at the wall boundary, and ρ_0 is the reference density, chosen to be unity.

Constant Dirichlet thermodynamic boundary conditions are based on the bounce-back rule for the non-equilibrium internal energy distribution [17]:

$$\bar{g}_\alpha^{neq} - \mathbf{e}_\alpha^2 \bar{f}_\alpha^{neq,iso} = - \left(\bar{g}_{\alpha^*}^{neq} - \mathbf{e}_{\alpha^*}^2 \bar{f}_{\alpha^*}^{neq,iso} \right). \quad (30)$$

where \mathbf{e}_α and \mathbf{e}_{α^*} have opposite directions. As was mentioned in [17], $\bar{f}_\alpha^{neq,iso}$ is the non-equilibrium density distribution function that neglects any heat flux contributions and is solely used to treat isothermal (*iso*) boundaries. The following relations for non-equilibrium are used: $\bar{f}_\alpha^{neq} = \bar{f}_\alpha - \bar{f}_\alpha^{eq}$ and $\bar{g}_\alpha^{neq} = \bar{g}_\alpha - \bar{g}_\alpha^{eq}$. Using these relations, an expression for \bar{g}_α^+ in Eq. (27) can be determined (see Appendix for further details). We arrive at the following formulation for the discontinuous Galerkin thermal boundary condition:

In the case of $\alpha = 1, 2, 3, 4$. Then,

$$\bar{g}_\alpha - \bar{g}_\alpha^+ = \begin{cases} \Theta_{\alpha,1-4} & \text{for } \mathbf{n} \cdot \mathbf{e}_\alpha < 0 \\ 0 & \text{for } \mathbf{n} \cdot \mathbf{e}_\alpha \geq 0 \end{cases} \quad (31)$$

and for $\alpha = 5, 6, 7, 8$:

$$\bar{g}_\alpha - \bar{g}_\alpha^+ = \begin{cases} \Theta_{\alpha,5-8} & \text{for } \mathbf{n} \cdot \mathbf{e}_\alpha < 0 \\ 0 & \text{for } \mathbf{n} \cdot \mathbf{e}_\alpha \geq 0 \end{cases} \quad (32)$$

where

$$\begin{aligned} \Theta_{\alpha,1-4} &= \bar{g}_\alpha + \bar{g}_{\alpha^*} - \frac{2\rho_0 e_b}{9} [3 + 4.5(\mathbf{e}_\alpha \cdot \mathbf{u}_b)^2 - 1.5(\mathbf{u}_b \cdot \mathbf{u}_b)] + t_\alpha \dot{Q} \delta t \\ &\quad - \mathbf{e}_\alpha^2 (\bar{f}_\alpha + \bar{f}_{\alpha^*}) + \mathbf{e}_\alpha^2 (2t_\alpha \rho_0 [1 + 4.5(\mathbf{e}_\alpha \cdot \mathbf{u}_b)^2 - 1.5(\mathbf{u}_b \cdot \mathbf{u}_b)]). \\ \Theta_{\alpha,5-8} &= \bar{g}_\alpha + \bar{g}_{\alpha^*} - \frac{2\rho_0 e_b}{36} [3 + 4.5(\mathbf{e}_\alpha \cdot \mathbf{u}_b)^2 - 1.5(\mathbf{u}_b \cdot \mathbf{u}_b)] + t_\alpha \dot{Q} \delta t \\ &\quad - \mathbf{e}_\alpha^2 (\bar{f}_\alpha + \bar{f}_{\alpha^*}) + \mathbf{e}_\alpha^2 (2t_\alpha \rho_0 [1 + 4.5(\mathbf{e}_\alpha \cdot \mathbf{u}_b)^2 - 1.5(\mathbf{u}_b \cdot \mathbf{u}_b)]). \end{aligned}$$

Because this is the thermal boundary condition, we note e_b is the prescribed internal energy at the boundary that simply translates to a Dirichlet temperature boundary condition. Further details on the boundary conditions can be found in the Appendix.

3.3. Spectral element discretizations

In this section, we describe the functional form of the test function $\phi_{\alpha,h}$. These functions are actually chosen from the space of one-dimensional Legendre–Lagrange interpolation polynomials that are formally given as [27]:

$$l_i(\xi) = N(N + 1)^{-1} (1 - \xi^2) L'_N(\xi) / (\xi - \xi_i) L_N(\xi_i) \quad \text{for } \xi \in [-1, 1], \quad (33)$$

where ξ_i are the Gauss–Lobatto–Legendre quadrature nodes and $L_N(\xi)$ is the N th-order Legendre polynomial. Our choice to use quadrilateral elements, Ω^e , to fill our two-dimensional computational domain, $\Omega = \cup_{e=1}^E \Omega^e$, enables us to benefit from the tensor-product basis that is created with Eq. (33). Each coordinate $(x, y) \in \Omega^e$ is mapped on the reference domain, $(\xi, \eta) \in I := [-1, 1]^2$, through the Gordon–Hall mapping [27]. The tensor-product structure of the reference element I allows us to define a two-dimensional basis, $\psi_{ij}(\xi, \eta) = l_i(\xi(x))l_j(\eta(y)) = \phi$. The equality to ϕ is used to make the functional form of the test functions clear to the reader. We now replace the test functions used in Eq. (24) with ψ_{ij} and write

$$\bar{f}_\alpha^N(\mathbf{x}, t)_h^e = \sum_{i,j=0}^N (\bar{f}_\alpha^N)_{ij} \psi_{ij} \quad \text{and} \quad \bar{g}_\alpha^N(\mathbf{x}, t)_h^e = \sum_{i,j=0}^N (\bar{g}_\alpha^N)_{ij} \psi_{ij} \tag{34}$$

which are the local approximate solutions \bar{f}_α^N and \bar{g}_α^N written as the finite expansion of the ψ_{ij} on Ω^e . $(\bar{f}_\alpha^N)_{ij} = f_\alpha^N(x_i, y_j, t)$ and $(\bar{g}_\alpha^N)_{ij} = g_\alpha^N(x_i, y_j, t)$ represent the approximate solution \bar{f}_α^N and \bar{g}_α^N on the nodal points (x_i, y_j) at time t . Plugging the approximate solutions of Eq. (34) into their respective weak formulations (i.e., Eqs (25) and (26)), we will then arrive at the following semi-discrete scheme:

$$\frac{d\bar{\mathbf{f}}_\alpha}{dt} + \mathbf{M}^{-1}\mathbf{D}\bar{\mathbf{f}}_\alpha = \mathbf{M}^{-1}\mathbf{R}_f\bar{\mathbf{f}}_\alpha, \tag{35}$$

$$\frac{d\bar{\mathbf{g}}_\alpha}{dt} + \mathbf{M}^{-1}\mathbf{D}\bar{\mathbf{g}}_\alpha = \mathbf{M}^{-1}\mathbf{R}_g\bar{\mathbf{g}}_\alpha, \tag{36}$$

where the solution vectors are defined by $\bar{\mathbf{f}}_\alpha = [(\bar{f}_\alpha^N)_{ij}]$ and $\bar{\mathbf{g}}_\alpha = [(\bar{g}_\alpha^N)_{ij}]$ on a local element. The mass matrix is defined as

$$\mathbf{M} = (\psi_{ij}, \psi_{ij})_{\Omega^e} = J(\hat{M} \otimes \hat{M}), \tag{37}$$

where $\hat{M}_{ii} = \sum_{k=0}^N l_i(\xi_k)l_i(\xi_k)w_k$ is the one-dimensional mass matrix with the quadrature weight w_k defined on the reference domain $[-1, 1]$ and $J = [J_{ll}] = \text{diag}\{J_{ij}\}$ represents the value of the Jacobian at each node (x_i, y_j) with $l = i + (N + 1)j$ on Ω^e . The one-dimensional mass matrix \hat{M} is diagonal because of the orthogonal property of the Legendre–Lagrange interpolation polynomials on the Gauss–Lobatto–Legendre nodes, and thus, the two-dimensional mass matrix \mathbf{M} is also diagonal. The gradient matrices are defined by

$$\mathbf{D} = e_{\alpha x}\mathbf{D}_x + e_{\alpha y}\mathbf{D}_y, \tag{38}$$

where the differentiation matrices can be represented by a tensor product form of the one-dimensional differentiation matrix $\hat{D} = [\hat{D}_{ii}] = l'_i(\xi_i)$ as

$$\mathbf{D}_x = \left(\frac{\partial \psi_{ij}}{\partial x}, \psi_{ij} \right) = G^{\xi x} J[\hat{M} \otimes \hat{M} \hat{D}] + G^{\eta x} J[\hat{M} \hat{D} \otimes \hat{M}], \tag{39}$$

$$\mathbf{D}_y = \left(\frac{\partial \psi_{ij}}{\partial y}, \psi_{ij} \right) = G^{\xi y} J[\hat{M} \otimes \hat{M} \hat{D}] + G^{\eta y} J[\hat{M} \hat{D} \otimes \hat{M}], \tag{40}$$

where $G^{\xi x}$, $G^{\xi y}$, $G^{\eta x}$, and $G^{\eta y}$ represent diagonal matrices for the geometric factors $\frac{\partial \xi}{\partial x}$, $\frac{\partial \xi}{\partial y}$, $\frac{\partial \eta}{\partial x}$, and $\frac{\partial \eta}{\partial y}$, respectively, at the nodal points (x_i, y_j) . The surface integrations acting on the boundary nodes on each face of the local element in Eqs (35)–(36) are represented by

$$\mathbf{R}_f \bar{\mathbf{f}}_\alpha = \sum_{s=1}^4 \sum_{k=0}^N \mathcal{R}_k^s \{ \mathbf{n} \cdot [\mathbf{F}_\alpha(\bar{f}) - \mathbf{F}_\alpha^*(\bar{f})] \} w_k J_k^s, \tag{41}$$

$$\mathbf{R}_g \bar{\mathbf{g}}_\alpha = \sum_{s=1}^4 \sum_{k=0}^N \mathcal{R}_k^s \{ \mathbf{n} \cdot [\mathbf{G}_\alpha(\bar{g}) - \mathbf{G}_\alpha^*(\bar{g})] \} w_k J_k^s, \tag{42}$$

where $\mathcal{R}_k^s \{ \cdot \}$ extracts the information of $\{ \cdot \}$ at the nodes situated on each face of the local element for the face number s and J_k^s is the surface Jacobian at the nodes on each face.

4. NUMERICAL RESULTS

In this section, we show computational results and validation for our proposed scheme. To begin, we compare our computations with analytical solutions for conjugate heat conduction between two solid materials with variable conductivity. Following this, we include fluid into our scheme by analyzing flow past a solid cylinder that volumetrically generates heat. Finally, we present conjugate natural convection results for flow in a horizontal annulus.

4.1. Accuracy for spectral-element discontinuous Galerkin thermal lattice Boltzmann method: steady-state conduction in a composite, two-layer annulus

We investigate the steady-state conduction of heat through a composite annulus that consists of two concentric circular annuli that are in perfect thermal contact. This problem is chosen to illustrate the benefit of the SEDG scheme that allows for our lattice Boltzmann computations to be performed on body-conforming meshes with irregular grid distributions. Figure 1 shows a schematic of the problem where each annulus has a unique thermal conductivity (κ) and diffusivity (χ). The problem is further defined by Dirichlet boundary conditions, T_1 and T_2 , which are maintained at the inner ($r = R_1$) and outer ($r = R_2$) boundaries, respectively. The analytical solution to this problem is given in polar coordinates:

$$T_{sol}^c(r) = \begin{cases} A^c \ln r + B^c & \text{for } R_1 \leq r \leq R_M, \\ C^c \ln r + D^c & \text{for } R_M \leq r \leq R_2. \end{cases} \tag{43}$$

where $A^c = \gamma C^c$, $B^c = T_1 - \gamma C^c \ln(R_1)$, $C^c = \frac{\Delta T}{(\gamma \ln(R_1/R_M) + \ln(R_M/R_2))}$, $D^c = T_2 - C^c \ln(R_2)$, and $\Delta T = T_2 - T_1$. For this study, we choose the conductivity ratio to be $\gamma = \frac{\kappa_2}{\kappa_1} = 10$ and 1000. Results from our calculations are shown in Figure 2. The results agree well with the steady-state analytical solution given earlier. Computations were performed using $N = 2, 4,$ and 6 order polynomials on a uniform mesh distribution with $E = 8 \times 8 = 64$ uniform elements, where eight

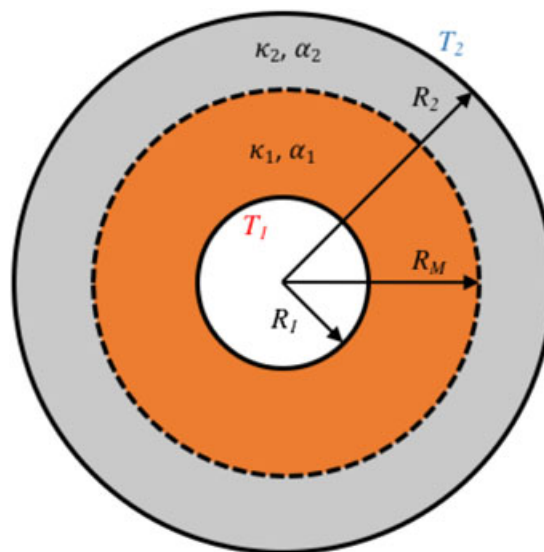


Figure 1. Schematic of a composite, two-layer annulus.

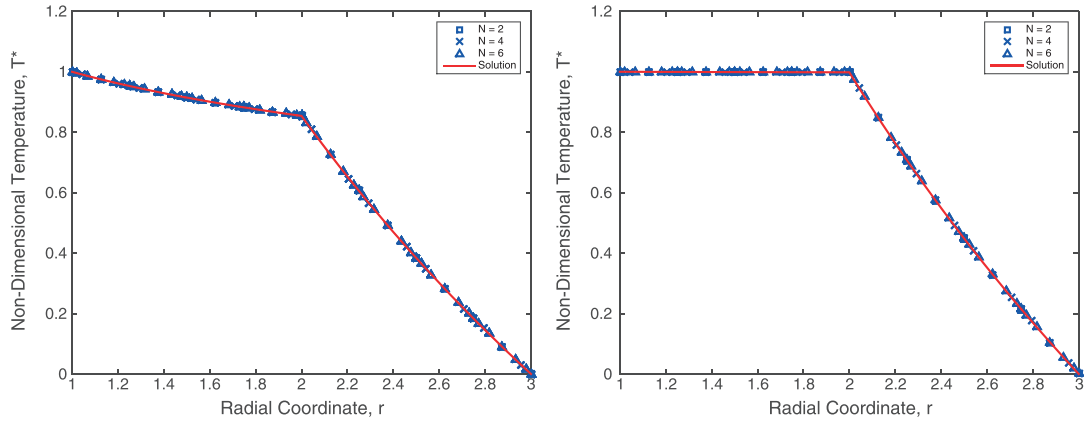


Figure 2. Steady-state temperature profiles for conduction in a composite, two-layer annulus. The plot on the left shows results for conductivity ratio $\gamma = 10$. The plot on the right shows results for conductivity ratio $\gamma = 1000$.

elements are uniformly distributed in the radial and azimuthal directions. Convergence of the solution is shown in Figure 3, where we show results for $\gamma = \frac{\kappa_2}{\kappa_1} = 10$ at $N = 2$ and $N = 3$. We compute the L_2 error in the following manner:

$$\|e_T\|_{\Omega} = \sqrt{\sum_{k=1}^K \|e_T\|_{\Omega^k}^2} \quad (44)$$

where K is the total number of elements. $e_T = T - T_{sol}^c$ is a pointwise calculation and the local L_2 norm, $\|\cdot\|_{\Omega^k}^2$ is given by

$$\|e_T\|_{\Omega^k}^2 = (e_T, e_T)_{\Omega^k} = \mathbf{e}_T^T \mathbf{M} \mathbf{e}_T \quad (45)$$

with $\mathbf{e}_T = [e_{T,1}^k, \dots, e_{T,(N+1)^2}^k]^T$ representing the vector of the local nodal solution. \mathbf{M} is the element mass-matrix defined by Eq. (37). The superscript T is the transpose operation on a vector. As a comparison, we include the second and third order lines into Figure 3 where we observe how the SEDG-based results follow the respective slopes.

4.2. Flow past a heated cylinder

We characterize forced convection flows with three non-dimensional numbers: the Reynolds number (Re), Prandtl number (Pr), and thermal conductivity ratio (γ) between the solid cylinder and fluid. They are defined as follows:

$$Re = \frac{U_i D}{\nu_f}, \quad Pr = \frac{\nu_f}{\chi_f}, \quad \text{and} \quad \gamma = \frac{\kappa_s}{\kappa_f}, \quad (46)$$

where U_i is the inflow boundary velocity in our simulation, D is the diameter of the cylinder, ν_f is the kinematic viscosity, and χ_f is the thermal diffusivity of the fluid. The characteristic velocity, U_i , is based upon the Mach number (Ma) in our simulation, which is chosen to be $Ma = U_i/c_s \approx 0.01$. Our choice for Re will vary from $Re = 5 - 40$, while we will keep fluid and solid properties (i.e., ν_f , κ_f , and κ_s) fixed and hence fix Pr and γ . Our aim is to simulate a situation where water is flowing past a heat-generating solid carbon steel cylinder. At 20°C , this means $Pr \approx 6$ and $\gamma \approx 90$. Table I shows the material properties for the fluid and cylinder. For forced convection flows, we set $\mathbf{F} = 0$ in Eq. (1) because flow phenomena is driven by the inlet boundary conditions.

The heat source term \dot{Q} is non-dimensionalized via the diffusive time scale $t \sim D^2/\chi_f$. We write the non-dimensionalized heat source term via

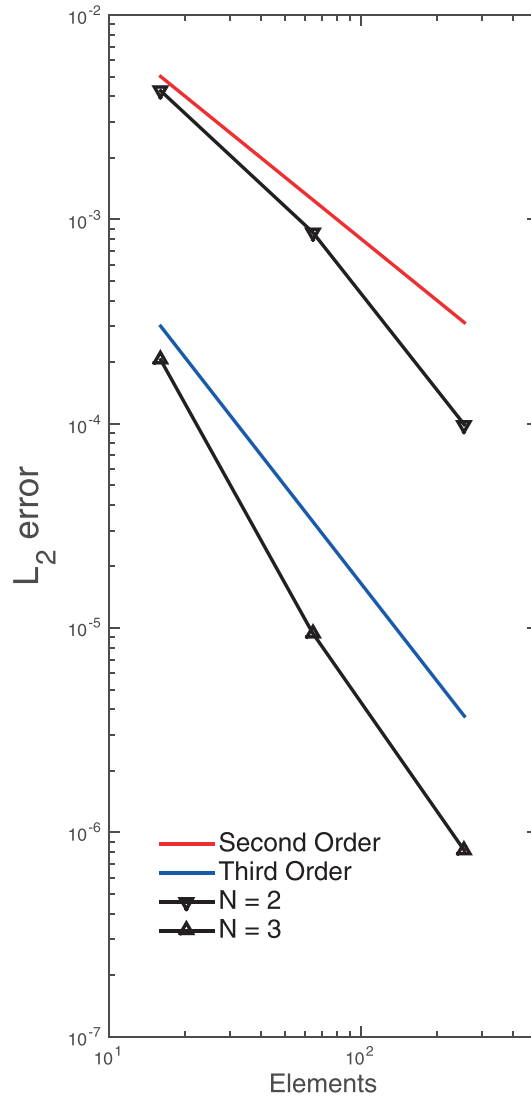


Figure 3. L_2 error for conjugate heat transfer in the two-layer annulus with conductivity ratio $\gamma = \frac{\kappa_2}{\kappa_1} = 10$. Computations were performed on three uniform mesh distributions: $E = 4 \times 4 = 16$, $E = 8 \times 8 = 64$, and $E = 16 \times 16 = 256$ uniform elements.

Table I. Material properties for fluid (water) [30] and cylinder (steel) [29].

Property at 20° C	Fluid (water)	Cylinder (steel)
Density (kg/m^3)	998.3	7833
Absolute viscosity ($kg/m \cdot s$)	1.0003×10^{-3}	—
Specific heat ($J/kg \cdot ^\circ C$)	4182	465
Thermal conductivity ($W/m \cdot ^\circ C$)	0.5996	54
Thermal diffusivity (m^2/s)	1.436×10^{-7}	1.474×10^{-5}

$$\dot{Q}^* = \frac{\dot{Q} D^2}{\kappa_f T_i} \quad (47)$$

with T_i being some characteristic temperature in the computational domain. The value that we use for this problem is given by $\dot{Q}^* \approx 5.5$.

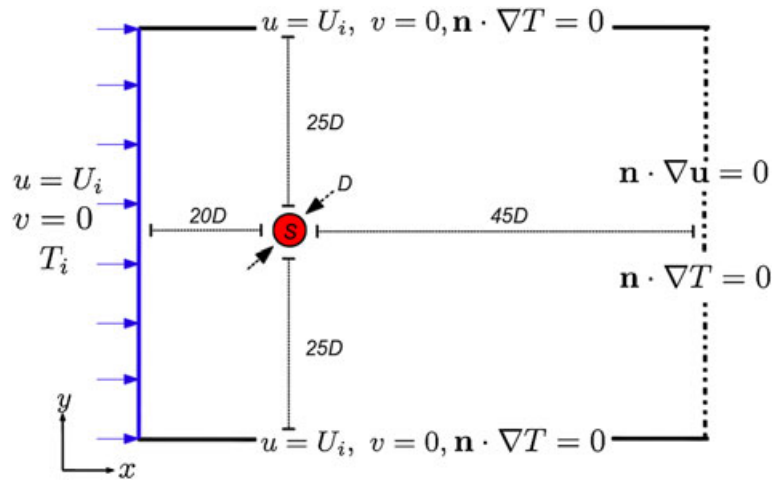


Figure 4. Schematic for the conjugate heat transfer of flow past a cylinder with heat source.

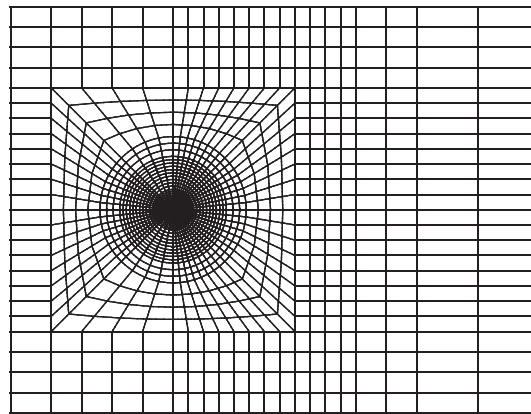


Figure 5. Mesh for the conjugate heat transfer of flow past a cylinder with heat source. Total number of elements is approximately 2100. Polynomial order is $N = 5$.

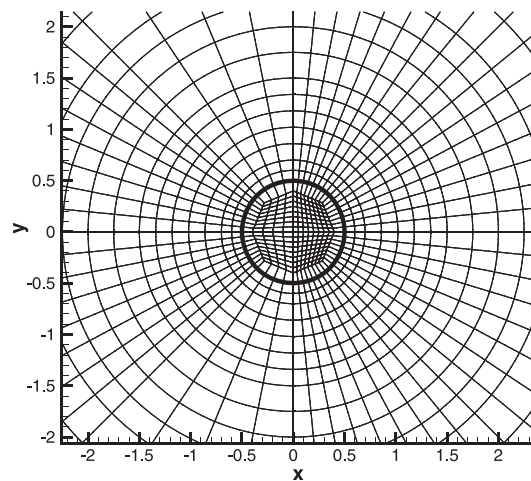


Figure 6. Mesh near the cylinder. Thicker black line represents the cylinder surface. Polynomial order is $N = 5$.

The schematic description to this problem is shown in Figure 4. At time, $t = 0$, there is a potential flow with the temperature in the entire computational domain to be T_i . The flow entering the domain is prescribed with a temperature T_i and velocity $\mathbf{u}_b = (U_i, 0)$. Figures 5 and 6 show the mesh that our computations are performed upon. The cylindrical surface is represented by a thicker black line as can be seen in Figure 6. We mesh within the cylinder and immediately downstream of the cylinder with additional refinement in order to capture the symmetric vortex structure that is created. The polynomial interpolation we employ is of order $N = 5$. Figure 7 shows the initial flow pattern that we employed for the simulation, which is a potential flow. This automatically introduces a slip velocity on the surface of the cylinder with a vortex sheet of zero thickness. At $t > 0$, we impose $\mathbf{u}_b = (0, 0)$ on the surface of the cylinder. Figures 8, 9, and 10 show steady-state streamlines and

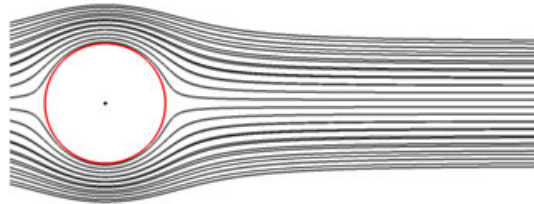


Figure 7. Streamlines of potential flow that represent the initial flow conditions. $t = 0$.

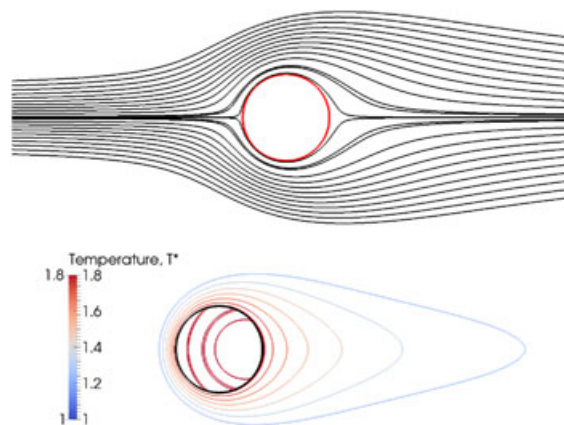


Figure 8. Steady-state ($t = \infty$) streamlines (top) and isotherms (bottom) for forced convection past a cylinder with heat-generating cylinder at $Re = 5$

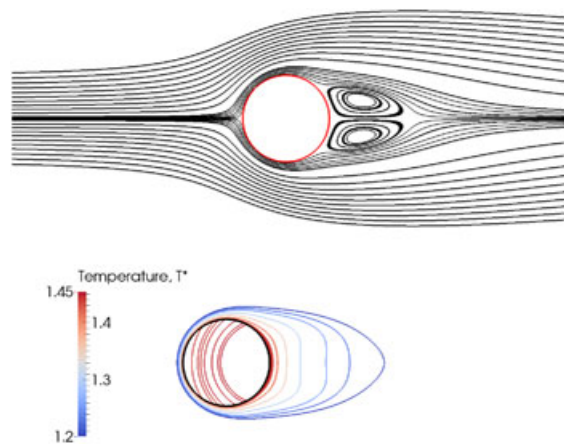


Figure 9. Steady-state ($t = \infty$) streamlines (top) and isotherms (bottom) for forced convection past a cylinder with heat-generating cylinder at $Re = 20$

isotherms for $Re = 5$, $Re = 20$, and $Re = 40$, respectively. We observe how the isotherm profile changes and is advected as the flow matures to its steady state. We also see how the hotter isotherms remain near to the heated cylinder while the cooler isotherms are advected and elongated further downstream of the cylinder. Upon further investigation, it is observed that the isotherms are cooling down as Re increases. Figure 11 shows the steady-state surface temperature distribution along the cylinder surface for $Re = 40$. Degrees are measured starting from 0 at the front (left) of the cylinder center and rotating counter-clockwise to 180, at the rear of the cylinder. We compare the SEDG-TLBM results against the Nek5000 results for the same polynomial order, $N = 5$. The average temperature difference between the two profiles is about a 0.3% error, so we believe the results agree well. We also plot the maximum temperature within the cylinder in Figure 12 that provides evidence to confirm that the temperature within the cylinder decreases as the Re increases. Because of the symmetry of the problem, the maximum temperature is located along the horizontal diameter of the circle. It is worthwhile to note that the maximum temperature location moves further away from the center, towards the rear of the cylinder as Re changes from 5 to 20. Between $Re = 20 - 40$, we see that this max. temperature location moves back towards the center. This is most likely owing to the separation region where a stronger reverse flow pulls in surrounding, cooler fluid, which impinges upon the rear of the cylinder. Similar results were found in [8].

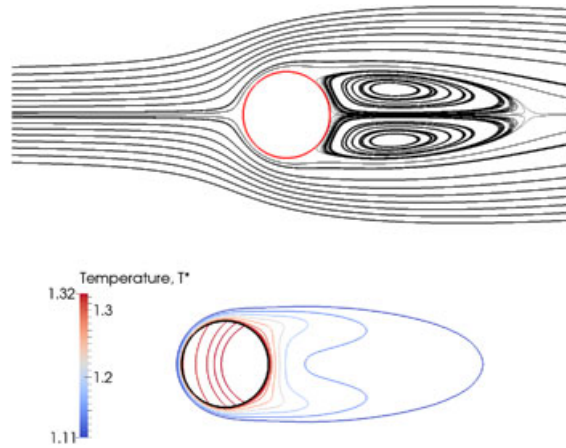


Figure 10. Steady-state ($t^* = \infty$) streamlines (top) and isotherms (bottom) for forced convection past a cylinder with heat generating cylinder at $Re = 40$

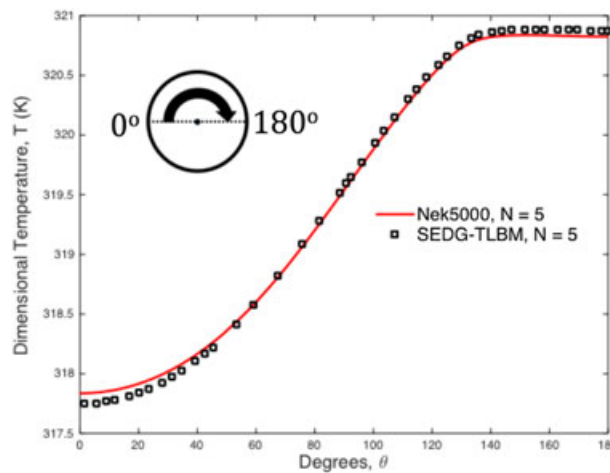


Figure 11. Steady-state dimensional temperature, T (K) along the upper half of cylindrical surface for $Re = 40$. The red line indicates the results from the Nek5000 Navier–Stokes solver.

The steady-state local Nusselt number along the cylindrical surface is plotted in Figure 13. We define Nu^* via

$$Nu^* = -\frac{D}{T_i} \left(\frac{\partial T}{\partial \mathbf{n}_{cyl}} \right)_{cylinder}, \tag{48}$$

where \mathbf{n}_{cyl} represents the outward pointing normal on the cylinder surface. Towards the front of the cylinder, we can observe that heat transfer increases with Re . This is because of the dominating convection effect that the fluid has over its own thermal diffusivity (i.e., Peclet number, $Pe = \frac{U_i D}{\chi_f} > 1$). As the fluid travels over the cylinder surface, the effect of Reynolds number plays a noticeable difference in the heat transfer. In particular, the heat flux towards the rear of the cylinder for $Re = 5$ is greater over the higher cases. This is most likely because of the absence of the vortex structure arising from the separation. At lower Re , the temperature of the cylinder is higher (especially towards the rear of the cylinder) and there is less of a reverse flow, which allows for higher heat flux to occur at the fluid–solid interface.

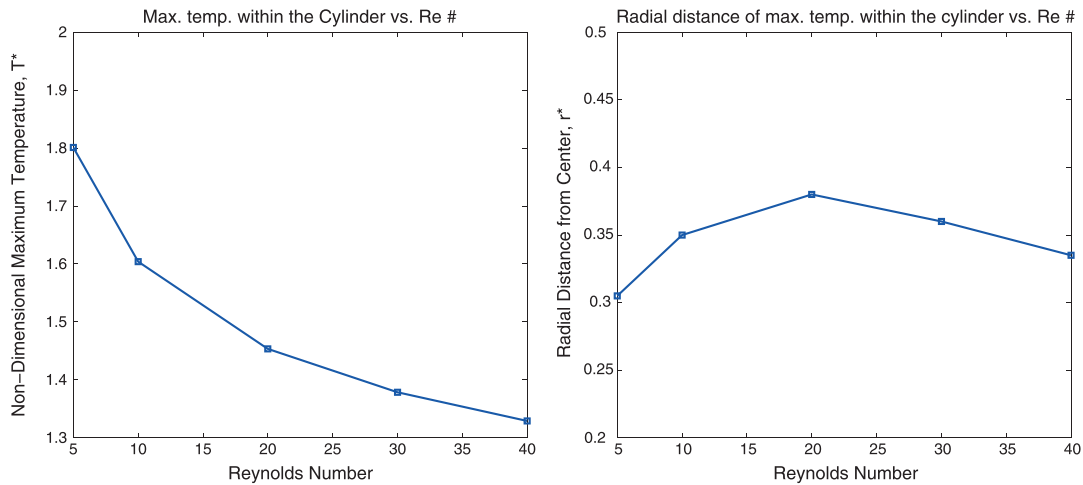


Figure 12. Maximum temperatures and respective distance from center of cylinder for $Re = 5 - 40$.

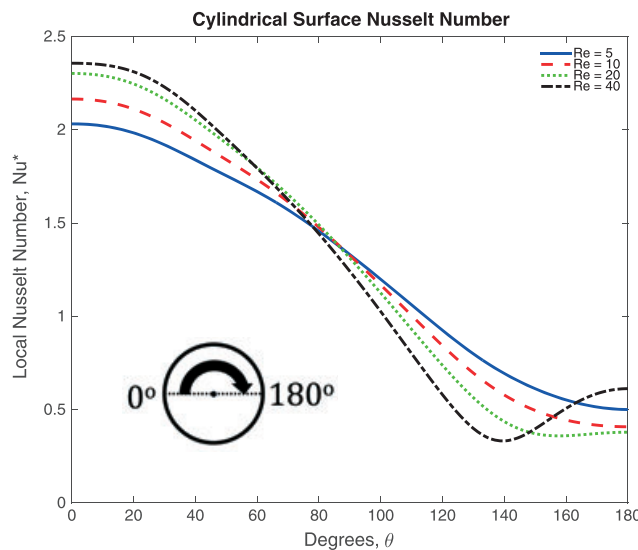


Figure 13. Steady-state local Nusselt numbers, Nu^* along upper half of cylindrical surface for $Re = 5 - 40$.

As Re increases, the separation region increases, thus trapping more fluid. At steady-state, the temperature in the cylinder decreases and the greater volume of fluid in this separation region allows for thermal heat transfer, whereby the temperature difference between the two mediums becomes smaller, thus decreasing the local heat flux. We also notice that the heat flux at the most rear location (180°) for $Re = 40$ is higher than the other cases. This, again, is probably due to the separation where the flow that impinges upon the cylinder at 180° is dominating the heat transfer process. This effect can be seen by the compression of isotherms in Figure 10 for the $Re = 40$ case.

4.3. Conjugate natural convection heat transfer in horizontal annuli

For natural convection flows, we consider a Boussinesq approximation [28] with a forcing term that is now included in Eqs (1) and (10). Details for this scheme are provided in [12] with the exception that the energy is now resolved according to Eq. (11) as opposed to a macroscopic equation. The formulation for the forcing term, \mathbf{F} , is defined as

$$\mathbf{F} = \rho \mathbf{g} \beta (T - T_o), \tag{49}$$

where T_o is a reference temperature, \mathbf{g} is the gravitational acceleration, and β is the thermal expansion coefficient. In accordance with the Boussinesq approximation, β is constant in space and time.

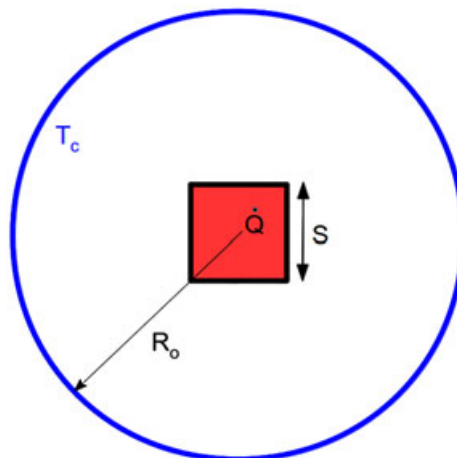


Figure 14. Schematic for the natural convection conjugate heat transfer within a horizontal annulus.

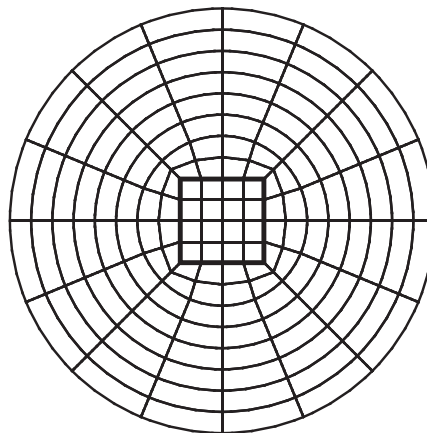


Figure 15. Mesh for the conjugate natural convection heat transfer of flow in horizontal annulus. Total number of elements is $E = 144$ with 16 elements approximating the solid square.

We characterize conjugate natural convection heat transfer with three non-dimensional numbers: the Grashof (Gr) number, the Prandtl number (Pr), and the conductivity ratio γ . Gr is given by

$$Gr = \frac{\beta |g| (\Delta T) L^3}{\nu_f^2} \quad (50)$$

where $\Delta T = \frac{\dot{Q} R_o^2}{\kappa_f}$. The Prandtl number (Pr) and the conductivity ratio γ are defined in Eq. (46).

The schematic description to this problem is shown in Figure 14. The inner region is a heat generating solid with a square cross-section and side length of S . The outer circular boundary is maintained at a constant temperature T_c , which represents our reference temperature T_o in Eq. (49). No-slip boundary conditions are imposed on the inner solid and outer boundaries. Initial conditions reflect a quiescent fluid where the temperature in the entire domain is T_c . The geometric parameter for this problem is given by aspect ratio $A = \frac{S}{2R_o} = 0.2$. At $t > 0$, heat generation within the solid square commences. Figure 15 shows the mesh distribution for this geometry where the thick black line represents the solid square boundary.

Figures 16 and 17 show the steady-state isotherms and streamlines for $Gr = 10^5$ and 10^6 . These results are based on $Pr = 0.708$ and $\gamma = 10$. The isotherms for $Gr = 10^5$ look nearly concentric about the center of the square, suggesting a conduction-dominated effect. In addition, streamlines are symmetric about the vertical axis revealing a kidney-shaped profile with the center of the streamlines located near the mid-horizontal plane. As the Gr number is increased to 10^6 , the center of the streamlines moves upwards and closer to the top of the annulus while symmetry is preserved. Isotherms now exhibit a plume-like structure emanating from the top of the square. Closely packed isotherms near the upper part of the outer cylinder and the lower part of the inner square suggest larger temperature gradients in these areas. As a means of further investigating the increased

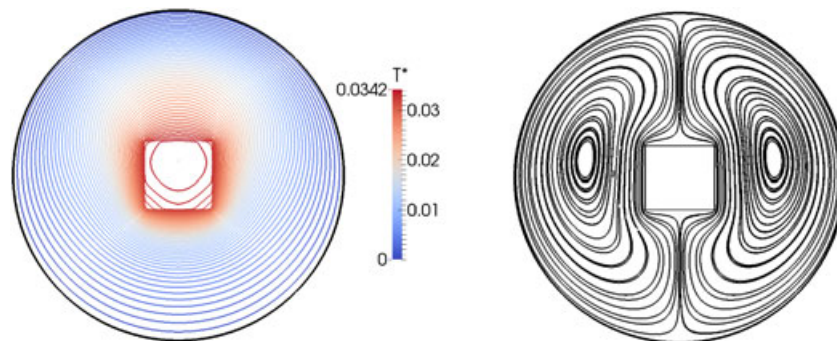


Figure 16. Isotherms (left) and streamlines (right) for $Gr = 10^5$, $Pr = 0.708$, and $\gamma = 10$. Results were obtained for polynomial order of $N = 5$.

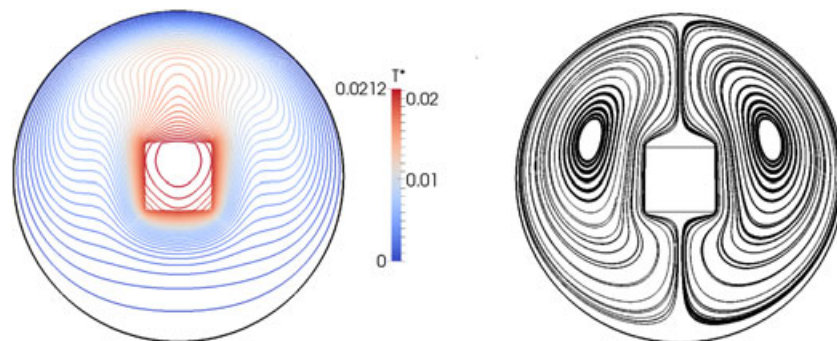


Figure 17. Isotherms (left) and streamlines (right) for $Gr = 10^6$, $Pr = 0.708$, and $\gamma = 10$. Results were obtained for polynomial order of $N = 5$.

Table II. Convergence of $Nu_{avg,ib}$ for $\gamma = 10$.

SEDG-TLBM (N)	$Gr = 10^5$	$Gr = 10^6$
3	3.08	4.85
5	3.07	4.95
7	3.07	4.97
9	3.07	4.98
Sambamurthy <i>et al.</i> [9]	≈ 3.00	≈ 5.00

temperature gradients, we compute the average Nusselt number of the inner boundary, $Nu_{av,ib}$ and compare results with the work carried out by Sambamurthy *et al.* [9]. $Nu_{av,ib}$ is calculated as

$$Nu_{av,ib} = \frac{S^*}{T_{av,ib}^* P_{ib}^*} \tag{51}$$

where S^* , P_{ib}^* , and $T_{av,ib}^*$ represent the non-dimensional length, perimeter, and average temperature, respectively, of the inner square boundary. Table II shows Nusselt number calculations for $Gr = 10^5$ and $Gr = 10^6$. As expected, the higher Nusselt number for $Gr = 10^6$ is due to the smaller thermal boundary layer that results from increased convection of flow. The results show the convergence of our scheme as polynomial order is increased from $N = 3$ to $N = 9$. The \approx symbol for the Sambamurthy *et al.* [9] results indicates an approximated value because the data were taken from graphical plots in their article. The results agree well with [9] and show reasonable accuracy at low polynomial order $N = 3$.

5. CONCLUSIONS

We have presented an SEDG-TLBM for solving fluid–solid CHT problems. Our method provides accurate results for CHT applications in complex geometries and hence can incorporate lattice Boltzmann-based boundary conditions in a relatively straightforward manner. Flow past a volumetrically heated solid cylinder is simulated using the SEDG-TLBM. As a first step, steady-state calculations are performed to exhibit the capabilities of the algorithm. By treating the computational domain as one medium with discontinuous material properties (i.e., thermal conductivities), temperature and heat flux continuity are ensured in our simulation with no additional work required to maintain these conditions at the solid–solid or fluid–solid interface. Calculations using the proposed thermal model have been carried out to investigate heat conduction in a two-layer annulus. In particular, we compare our computations with the analytical solution for a variety of polynomial orders. We also examine the situation where water is flowing past a solid heat-conducting carbon cylinder for $Re = 5 - 40$ with conductivity ratio of $\gamma \approx 90$. In each case, we observe a cooling of the cylinder as Re increases. In addition, we carry out conjugate natural convection in an annulus for $Gr = 10^5$ and $Gr = 10^6$. The average Nusselt number $Nu_{avg,ib}$ is computed, and we notice reasonable agreement with benchmark studies for low polynomial order N .

APPENDIX

In this Appendix, we provide more details on the derivation of the thermal boundary conditions described in Eqs (31) and (32). Using the relations, $\bar{f}_\alpha^{neq} = \bar{f}_\alpha - \bar{f}_\alpha^{eq}$ and $\bar{g}_\alpha^{neq} = \bar{g}_\alpha - \bar{g}_\alpha^{eq}$, we may write Eq. (30) as the following:

$$\bar{g}_\alpha - \bar{g}_\alpha^{eg} = -(\bar{g}_{\alpha^*} - \bar{g}_{\alpha^*}^{eq}) + \mathbf{e}_\alpha^2 (\bar{f}_\alpha - \bar{f}_\alpha^{eq}) + \mathbf{e}_{\alpha^*}^2 (\bar{f}_{\alpha^*} - \bar{f}_{\alpha^*}^{eq}), \tag{A.1}$$

noting that $\mathbf{e}_\alpha = -\mathbf{e}_{\alpha^*}$ and $\mathbf{e}_\alpha^2 = \mathbf{e}_{\alpha^*}^2$, Eq. (A.1) can be rearranged as

$$\bar{g}_\alpha = -\bar{g}_{\alpha^*} + (\bar{g}_\alpha^{eq} + \bar{g}_{\alpha^*}^{eg}) + \mathbf{e}_\alpha^2 (\bar{f}_\alpha + \bar{f}_{\alpha^*}) - \mathbf{e}_\alpha^2 (\bar{f}_\alpha^{eq} + \bar{f}_{\alpha^*}^{eq}) \tag{A.2}$$

For $\alpha = 1, 2, \dots, 8$;

$$\bar{f}_\alpha^{eq} + \bar{f}_{\alpha^*}^{eq} = 2t_\alpha \rho_0 [1 + 4.5(\mathbf{e}_\alpha \cdot \mathbf{u}_b)^2 - 1.5(\mathbf{u}_b \cdot \mathbf{u}_b)], \tag{A.3}$$

For $\alpha = 1, 2, 3, 4$;

$$\bar{g}_\alpha^{eq} + \bar{g}_{\alpha^*}^{eq} = \frac{2\rho_0 e_b}{9} [1.5 + 4.5(\mathbf{e}_\alpha \cdot \mathbf{u}_b)^2 - 1.5(\mathbf{u}_b \cdot \mathbf{u}_b)] - t_\alpha \dot{Q} \delta t, \tag{A.4}$$

For $\alpha = 5, 6, 7, 8$;

$$\bar{g}_\alpha^{eq} + \bar{g}_{\alpha^*}^{eq} = \frac{2\rho_0 e_b}{36} [3 + 4.5(\mathbf{e}_\alpha \cdot \mathbf{u}_b)^2 - 1.5(\mathbf{u}_b \cdot \mathbf{u}_b)] - t_\alpha \dot{Q} \delta t, \tag{A.5}$$

Substituting Eqs (A.3), (A.4), and (A.5) into (A.2), we have

For $\alpha = 1, 2, 3, 4$;

$$\begin{aligned} \bar{g}_\alpha = & -\bar{g}_{\alpha^*} + \frac{2\rho_0 e_b}{9} [1.5 + 4.5(\mathbf{e}_\alpha \cdot \mathbf{u}_b)^2 - 1.5(\mathbf{u}_b \cdot \mathbf{u}_b)] - t_\alpha \dot{Q} \delta t \\ & + \mathbf{e}_\alpha^2 (\bar{f}_\alpha + \bar{f}_{\alpha^*}) - \mathbf{e}_\alpha^2 (2t_\alpha \rho_0 [1 + 4.5(\mathbf{e}_\alpha \cdot \mathbf{u}_b)^2 - 1.5(\mathbf{u}_b \cdot \mathbf{u}_b)]), \end{aligned}$$

For $\alpha = 5, 6, 7, 8$;

$$\begin{aligned} \bar{g}_\alpha = & -\bar{g}_{\alpha^*} + \frac{2\rho_0 e_b}{36} [3 + 4.5(\mathbf{e}_\alpha \cdot \mathbf{u}_b)^2 - 1.5(\mathbf{u}_b \cdot \mathbf{u}_b)] - t_\alpha \dot{Q} \delta t \\ & + \mathbf{e}_\alpha^2 (\bar{f}_\alpha + \bar{f}_{\alpha^*}) - \mathbf{e}_\alpha^2 (2t_\alpha \rho_0 [1 + 4.5(\mathbf{e}_\alpha \cdot \mathbf{u}_b)^2 - 1.5(\mathbf{u}_b \cdot \mathbf{u}_b)]). \end{aligned}$$

Upon substitution of the aforementioned expressions into \bar{g}_α^+ , we arrive at the expressions given by Eqs (31) and (32).

The following are specific formulations based on the microscopic directions α and α^* :

if $\mathbf{e}_1 \cdot \mathbf{n} < 0$ ($\Leftrightarrow \mathbf{e}_3 \cdot \mathbf{n} > 0$); $\bar{g}_1 - \bar{g}_1^+ = [\bar{g}_1 + \bar{g}_3]$

$$- \frac{2\rho_0 e_b}{9} [1.5 + 4.5(\mathbf{e}_1 \cdot \mathbf{u}_b)^2 - 1.5(\mathbf{u}_b \cdot \mathbf{u}_b)] + t_1 \dot{Q} \delta t + \mathbf{e}_1^2 (\bar{f}_1 + \bar{f}_3)$$

$$- \mathbf{e}_1^2 (2t_1 \rho_0 [1 + 4.5(\mathbf{e}_1 \cdot \mathbf{u}_b)^2 - 1.5(\mathbf{u}_b \cdot \mathbf{u}_b)]), \bar{g}_3 - \bar{g}_3^+ = [\bar{g}_3 - \bar{g}_1] = 0,$$

if $\mathbf{e}_2 \cdot \mathbf{n} < 0$ ($\Leftrightarrow \mathbf{e}_4 \cdot \mathbf{n} > 0$); $\bar{g}_2 - \bar{g}_2^+ = [\bar{g}_2 + \bar{g}_4]$

$$- \frac{2\rho_0 e_b}{9} [1.5 + 4.5(\mathbf{e}_2 \cdot \mathbf{u}_b)^2 - 1.5(\mathbf{u}_b \cdot \mathbf{u}_b)] + t_2 \dot{Q} \delta t + \mathbf{e}_2^2 (\bar{f}_2 + \bar{f}_4)$$

$$- \mathbf{e}_2^2 (2t_2 \rho_0 [1 + 4.5(\mathbf{e}_2 \cdot \mathbf{u}_b)^2 - 1.5(\mathbf{u}_b \cdot \mathbf{u}_b)]), \bar{g}_4 - \bar{g}_4^+ = [\bar{g}_4 - \bar{g}_2] = 0,$$

if $\mathbf{e}_3 \cdot \mathbf{n} < 0$ ($\Leftrightarrow \mathbf{e}_1 \cdot \mathbf{n} > 0$); $\bar{g}_3 - \bar{g}_3^+ = [\bar{g}_3 + \bar{g}_1]$

$$- \frac{2\rho_0 e_b}{9} [1.5 + 4.5(\mathbf{e}_3 \cdot \mathbf{u}_b)^2 - 1.5(\mathbf{u}_b \cdot \mathbf{u}_b)] + t_3 \dot{Q} \delta t + \mathbf{e}_3^2 (\bar{f}_3 + \bar{f}_1)$$

$$- \mathbf{e}_3^2 (2t_3 \rho_0 [1 + 4.5(\mathbf{e}_3 \cdot \mathbf{u}_b)^2 - 1.5(\mathbf{u}_b \cdot \mathbf{u}_b)]), \bar{g}_1 - \bar{g}_1^+ = [\bar{g}_1 - \bar{g}_3] = 0,$$

if $\mathbf{e}_4 \cdot \mathbf{n} < 0$ ($\Leftrightarrow \mathbf{e}_2 \cdot \mathbf{n} > 0$); $\bar{g}_4 - \bar{g}_4^+ = [\bar{g}_4 + \bar{g}_2]$

$$- \frac{2\rho_0 e_b}{9} [1.5 + 4.5(\mathbf{e}_4 \cdot \mathbf{u}_b)^2 - 1.5(\mathbf{u}_b \cdot \mathbf{u}_b)] + t_4 \dot{Q} \delta t + \mathbf{e}_4^2 (\bar{f}_2 + \bar{f}_4)$$

$$- \mathbf{e}_4^2 (2t_4 \rho_0 [1 + 4.5(\mathbf{e}_4 \cdot \mathbf{u}_b)^2 - 1.5(\mathbf{u}_b \cdot \mathbf{u}_b)]), \bar{g}_2 - \bar{g}_2^+ = [\bar{g}_2 - \bar{g}_4] = 0,$$

if $\mathbf{e}_5 \cdot \mathbf{n} < 0$ ($\Leftrightarrow \mathbf{e}_7 \cdot \mathbf{n} > 0$); $\bar{g}_5 - \bar{g}_5^+ = [\bar{g}_5 + \bar{g}_7]$

$$- \frac{2\rho_0 e_b}{36} [3.0 + 4.5(\mathbf{e}_5 \cdot \mathbf{u}_b)^2 - 1.5(\mathbf{u}_b \cdot \mathbf{u}_b)] + t_5 \dot{Q} \delta t + \mathbf{e}_5^2 (\bar{f}_5 + \bar{f}_7)$$

$$- \mathbf{e}_5^2 (2t_5 \rho_0 [1 + 4.5(\mathbf{e}_5 \cdot \mathbf{u}_b)^2 - 1.5(\mathbf{u}_b \cdot \mathbf{u}_b)]), \bar{g}_7 - \bar{g}_7^+ = [\bar{g}_7 - \bar{g}_5] = 0,$$

if $\mathbf{e}_6 \cdot \mathbf{n} < 0$ ($\Leftrightarrow \mathbf{e}_8 \cdot \mathbf{n} > 0$); $\bar{g}_6 - \bar{g}_6^+ = [\bar{g}_6 + \bar{g}_8]$

$$- \frac{2\rho_0 e_b}{36} [3.0 + 4.5(\mathbf{e}_6 \cdot \mathbf{u}_b)^2 - 1.5(\mathbf{u}_b \cdot \mathbf{u}_b)] + t_6 \dot{Q} \delta t + \mathbf{e}_6^2 (\bar{f}_6 + \bar{f}_8)$$

$$- \mathbf{e}_6^2 (2t_6 \rho_0 [1 + 4.5(\mathbf{e}_6 \cdot \mathbf{u}_b)^2 - 1.5(\mathbf{u}_b \cdot \mathbf{u}_b)]), \bar{g}_8 - \bar{g}_8^+ = [\bar{g}_8 - \bar{g}_6] = 0,$$

if $\mathbf{e}_7 \cdot \mathbf{n} < 0$ ($\Leftrightarrow \mathbf{e}_5 \cdot \mathbf{n} > 0$); $\bar{g}_7 - \bar{g}_7^+ = [\bar{g}_7 + \bar{g}_5]$

$$- \frac{2\rho_0 e_b}{36} [3.0 + 4.5(\mathbf{e}_7 \cdot \mathbf{u}_b)^2 - 1.5(\mathbf{u}_b \cdot \mathbf{u}_b)] + t_7 \dot{Q} \delta t + \mathbf{e}_7^2 (\bar{f}_7 + \bar{f}_5)$$

$$- \mathbf{e}_7^2 (2t_7 \rho_0 [1 + 4.5(\mathbf{e}_7 \cdot \mathbf{u}_b)^2 - 1.5(\mathbf{u}_b \cdot \mathbf{u}_b)]), \bar{g}_5 - \bar{g}_5^+ = [\bar{g}_5 - \bar{g}_7] = 0,$$

if $\mathbf{e}_8 \cdot \mathbf{n} < 0$ ($\Leftrightarrow \mathbf{e}_6 \cdot \mathbf{n} > 0$); $\bar{g}_8 - \bar{g}_8^+ = [\bar{g}_8 + \bar{g}_6]$

$$- \frac{2\rho_0 e_b}{36} [3.0 + 4.5(\mathbf{e}_8 \cdot \mathbf{u}_b)^2 - 1.5(\mathbf{u}_b \cdot \mathbf{u}_b)] + t_8 \dot{Q} \delta t + \mathbf{e}_8^2 (\bar{f}_8 + \bar{f}_6)$$

$$- \mathbf{e}_8^2 (2t_8 \rho_0 [1 + 4.5(\mathbf{e}_8 \cdot \mathbf{u}_b)^2 - 1.5(\mathbf{u}_b \cdot \mathbf{u}_b)]), \bar{g}_6 - \bar{g}_6^+ = [\bar{g}_6 - \bar{g}_8] = 0.$$

ACKNOWLEDGEMENTS

This work is supported in part by the US Department of Energy, Office of Nuclear Energy’s Nuclear Energy University Programs, and in part by the US Department of Energy, under Contract DE-ACO2-O6CH11357. We also thank Kalu Chibueze Uga for his help in formulating the thermal boundary condition.

REFERENCES

1. Merzari E, Pointer WD, Smith JG, Tentner A, Fischer P. Numerical simulation of the flow in wire-wrapped pin bundles: effect of pin-wire contact modeling. *Nuclear Engineering and Design* 2012; **253**:374–386.
2. Karniadakis GE. Numerical simulation of forced convection heat transfer from a cylinder in crossflow. *International Journal of Heat and Mass Transfer* 1988; **31**:107–118.
3. Lange CF, Durst F, Breuer M. Momentum and heat transfer from cylinders in laminar crossflow at $10^{-4} \leq Re \leq 200$. *International Journal of Heat and Mass Transfer* 1998; **41**:3409–3430.
4. Wang J, Wang M, Li Z. A lattice Boltzmann algorithm for fluid–solid conjugate heat transfer. *International Journal of Thermal Sciences* 2007; **46**:228–234.
5. Jain PC, Goel BS. A numerical study of unsteady laminar forced convection from a circular cylinder. *Journal of Heat Transfer* 1976; **98**:303–307.
6. Juncu G. Unsteady conjugate heat/mass transfer from a circular cylinder in laminar crossflow at low Reynolds numbers. *International Journal of Heat and Mass Transfer* 2004; **47**:2469–2480.
7. Das MK, Reddy KS. Conjugate natural convection heat transfer in an inclined square cavity containing a conducting block. *International Journal of Heat and Mass Transfer* 2006; **49**:4987–5000.
8. Jeon BJ, Kim YS, Choi HG. Effect of the Reynolds number on the conjugate heat transfer around a circular cylinder with heat source. *Journal of Mechanical Science and Technology* 2012; **26**:3849–3855.
9. Sambamurthy NB, Shaija A, Narasimham GS, et al. Laminar conjugate natural convection in horizontal annuli. *International Journal of Heat and Fluid Flow* 2008; **29**:1347–1359.
10. Chen S, Doolen GD. Lattice Boltzmann method for fluid flows. *Annual Review of Fluid Mechanics* 1998; **30**: 329–364.
11. Guo Z, Zheng C, Shi B, et al. Thermal lattice Boltzmann equation for low Mach number flows: decoupling model. *Physical Review E* 2007; **75**:036704.
12. Patel SS, Min M, Uga KC, et al. A spectral-element discontinuous Galerkin lattice Boltzmann method for simulating natural convection heat transfer in a horizontal concentric annulus. *Computers & Fluids* 2014; **95**:197–209.
13. Jami M, Mezrhab A, Bouzidi MH, et al. Lattice Boltzmann method applied to the laminar natural convection in an enclosure with a heat-generating cylinder conducting body. *International Journal of Thermal Sciences* 2007; **46**: 38–47.

14. Yan YY, Zu YQ. Numerical simulation of heat transfer and fluid flow past a rotating isothermal cylinder – a LBM approach. *International Journal of Heat and Mass Transfer* 2008; **51**:2519–2536.
15. Min M, Lee T. A spectral-element discontinuous Galerkin lattice Boltzmann method for nearly incompressible flows. *Journal of Computational Physics* 2011; **230**:245–259.
16. Shan X, Chen H. Lattice Boltzmann model for simulating flows with multiple phases and components. *Physical Review E* 1993; **47**:1815–1819.
17. He X, Chen S, Doolen GD. A novel thermal model for the lattice Boltzmann method in incompressible limit. *Journal of Computational Physics* 1998; **146**:282–300.
18. Fischer P, Lottes J, Pointer D, Siegel A. Petascale algorithms for reactor hydrodynamics. *Journal of Physics: Conference Series* 2008; **125**:012076. IOP Publishing.
19. Bhatnagar PL, Gross EP, Krook M. Model for collision processes in gases. I. Small amplitude processes in charged and neutral one-component systems. *Physical review* 1954; **94**:511.
20. Alexander FJ, Chen S, Sterling JD. Lattice Boltzmann thermohydrodynamics. *Physical Review E* 1993; **47**:R2249.
21. Peng Y, Shu C, Chew YT. Simplified thermal lattice Boltzmann model for incompressible thermal flows. *Physical Review E* 2003; **026701**:68.
22. Qian Y H, d'Humires D, Lallemand P. Lattice BGK models for Navier–Stokes equation. *Europhysics Letters* 1992; **17**:479–484.
23. He X, Shan X, Doolen GD. Discrete Boltzmann equation model for nonideal gases. *Physical Review E* 1998; **57**:R13.
24. Lee T, Lin CL. An Eulerian description of the streaming process in the lattice Boltzmann equation. *Journal of Computational Physics* 2003; **185**:445–471.
25. Hesthaven JS, Warburton T. *Nodal Discontinuous Galerkin Methods, Algorithms, Analysis, and Applications*. Springer Science and Business Media: New York, NY, 2008.
26. Zou Q, He X. On pressure and velocity boundary conditions for the lattice Boltzmann BGK model. *Physics of Fluids* 1997; **9**:1591–1598.
27. Deville MO, Fischer PF, Mund EH. *High-order Methods for Incompressible Fluid Flow*. Cambridge University Press: Cambridge, UK, 2002.
28. Shan X. Simulation of Rayleigh–Bénard convection using a lattice Boltzmann method. *Physical Review E* 1997; **55**:2780–2788.
29. Ozisik MN. *Heat conduction*. John Wiley & Sons: Hoboken, NJ, 1993.
30. Jiji L M, Jiji LM. *Heat Convection*. Springer: New York, 2006.